Future Change of Northern Hemisphere Summer Tropical–Extratropical Teleconnection in CMIP5 Models*

JUNE-YI LEE,[+] BIN WANG,[#] KYONG-HWAN SEO,[+] JONG-SEONG KUG,[@,&] YONG-SANG CHOI,[**] YU KOSAKA,[++] AND KYUNG-JA HA[+]

[+] *Department of Atmospheric Sciences, Pusan National University, Busan, South Korea*
[#] *International Pacific Research Center, and Department of Meteorology, University of Hawai'i at Mānoa, Honolulu, Hawaii*
[@] *Korea Institute of Ocean Science and Technology, Ansan, South Korea*
[**] *Ewha Womans University, Seoul, South Korea*
[++] *Scripps Institution of Oceanography, University of California, San Diego, La Jolla, California*

(Manuscript received 1 May 2013, in final form 24 January 2014)

ABSTRACT

Two dominant global-scale teleconnections in the Northern Hemisphere (NH) extratropics during boreal summer season (June–August) have been identified: the western North Pacific–North America (WPNA) and circumglobal teleconnection (CGT) patterns. These teleconnection patterns are of critical importance for the NH summer seasonal climate prediction. Here, how these teleconnections will change under anthropogenic global warming is investigated using representative concentration pathway 4.5 (RCP4.5) experiments by 20 coupled models that participated in phase 5 of the Coupled Model Intercomparison Project (CMIP5). The six best models are selected based on their performance in simulation of the two teleconnection patterns and climatological means and variances of atmospheric circulation, precipitation, and sea surface temperature. The selected models capture the CGT and its relationship with the Indian summer monsoon (ISM) reasonably well. The models can also capture the WPNA circulation pattern but with striking deficiencies in reproducing its associated rainfall anomalies due to poor simulation of the western North Pacific summer monsoon rainfall. The following changes are anticipated in the latter half of twenty-first century under the RCP4.5 scenario: 1) significant weakening of year-to-year variability of the upper-level circulation due to increased atmospheric stability, although the moderate increase in convective heating over the tropics may act to strengthen the variability; 2) intensification of the WPNA pattern and major spectral peaks, particularly over the eastern Pacific–North America and North Atlantic–Europe sectors, which is attributed to the strengthening of its relationship with the preceding mature phase of El Niño–Southern Oscillation (ENSO); and 3) weakening of the CGT due to atmospheric stabilization and decreasing relationship with ISM as well as weakening of the ISM–ENSO relationship.

1. Introduction

The tropical–extratropical teleconnections in the Northern Hemisphere (NH) during boreal summer have recently received much attention, because these teleconnections have a global impact by linking convective heating anomalies over the western North Pacific and South Asian monsoon region with the NH circulation anomalies (e.g., Ding and Wang 2005; Ding et al. 2011; Lee et al. 2011). Two dominant teleconnections have been identified as shown in Fig. 1a by applying empirical orthogonal function (EOF) analysis to 200-hPa

* School of Ocean and Earth Science and Technology Publication Number 9071 and International Pacific Research Center Publication Number 1043.

[&] Current affiliation: School of Environmental Science and Engineering, Pohang University of Science and Technology, Pohang, South Korea.

Corresponding author address: Dr. Kyong-Hwan Seo, Department of Atmospheric Sciences, Pusan National University, Busan 609-735, South Korea.
E-mail: khseo@pusan.ac.kr

DOI: 10.1175/JCLI-D-13-00261.1

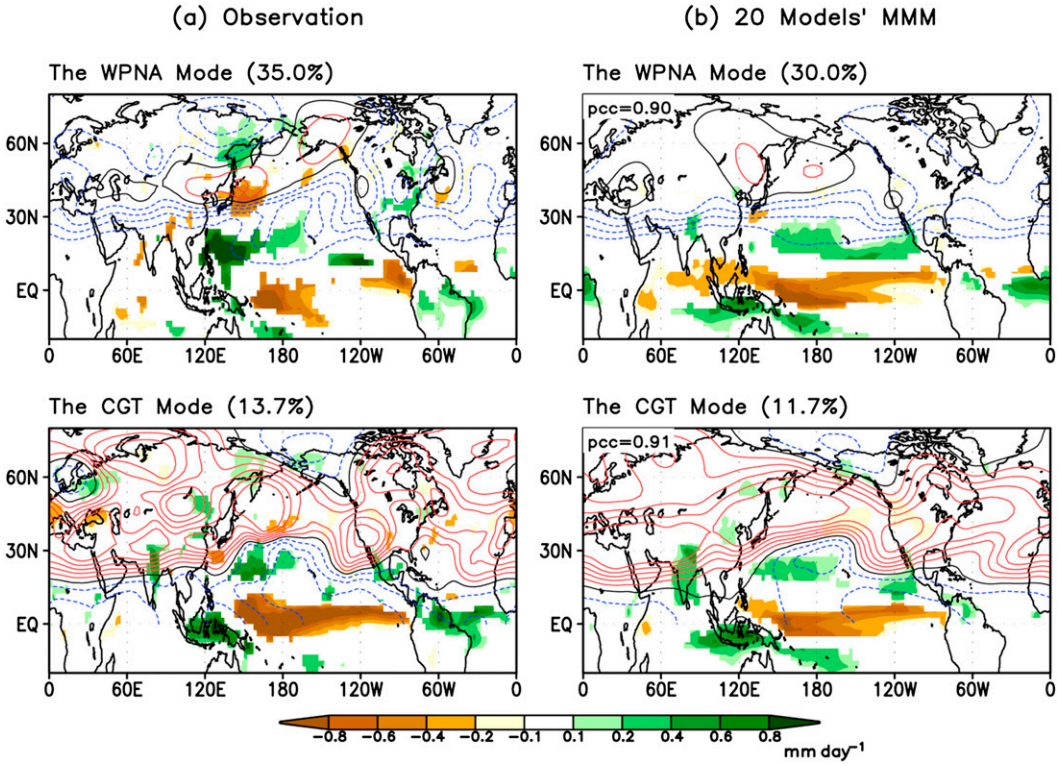

FIG. 1. Spatial patterns (contour) of the WPNA and CGT mode in (a) observations and (b) the 20-model MMM obtained from EOF analysis of Z200 anomalies for the period of 1979–2008. The regressed JJA precipitation anomalies against the corresponding principal component that exceed a statistical significant test at 95% confidence level are shaded.

geopotential height (Z200) anomaly during boreal summer. One is the circumglobal teleconnection (CGT) pattern represented by the second EOF mode that appears preferentially in summers preceding the peak phase of El Niño–Southern Oscillation (ENSO) cycle in association with the Indian summer monsoon (ISM) rainfall anomaly (Ding and Wang 2005). The other is the western North Pacific–North America (WPNA) pattern captured by the first EOF mode that tends to occur in summers following ENSO peak phases in association with the western North Pacific summer monsoon (WNPSM) rainfall anomaly (Ding et al. 2011).

The teleconnections in boreal summer season are weaker than their winter counterpart because of a weaker westerly jet with the northward shift. However, they are intimately related to surface climate anomalies, thus acting as a significant source of climate variability and predictability over the NH extratropics on intraseasonal (Ding and Wang 2007; Lee et al. 2013; Moon et al. 2013) and seasonal time scales (Wang et al. 2009; Lee et al. 2010, 2011; Ha et al. 2012; Jia et al. 2012). In particular, seasonal prediction skill for the boreal summer NH upper-level circulation mainly comes from the numerical models' ability to predict the WPNA and CGT modes (Lee et al. 2011; Lee and Wang 2012). Current coupled models are able to predict both spatial and temporal characteristics of the WPNA and CGT modes 1 month ahead with high fidelity, although they have difficulty in capturing details of the prominent wavelike structures of the observed CGT (Lee et al. 2011).

Wang et al. (2012) demonstrated that the CGT has experienced a significant interdecadal change since late 1970s as a consequence of 1) weakened coupling between the ISM rainfall and midlatitude circulation associated with changes in ENSO properties and 2) the southward shift of upper-level westerlies over the North Atlantic and Europe that tends to enhance coupling between the West African summer monsoon rainfall and midlatitude circulation. In particular, changes in ENSO characteristics since the late 1970s that include frequency, intensity, structure, and propagation (Wang 1995, Gu and Philander 1997; Wallace et al. 1998; An and Wang 2000) have played an important role in changes of the interannual variability of the ENSO–Asian summer monsoon relationship (Wang et al. 2008) and the NH atmospheric variability and predictability (Jia et al. 2014a,b).

The effect of anthropogenic forcing on ENSO characteristics have been studied by analyzing the phase 3 of

the Coupled Model Intercomparison Project (CMIP3) models (Collins 2005; Guilyardi 2006; Meehl et al. 2007; Yeh et al. 2009; Latif and Keenlyside 2009; Collins et al. 2010) and the phase 5 (CMIP5) models (Kim and Yu 2012; Guilyardi et al. 2012; Stevenson et al. 2012; Weare 2013; Chu et al. 2014). Most of CMIP3 and CMIP5 models project robust El Niño–like warming in the tropical Pacific (i.e., Collins 2005; Latif and Keenlyside 2009; Guilyardi et al. 2012; and many others). However, the CMIP5 coupled general circulation models (CGCMs) tend to show diverse results in ENSO variability changes (Guilyardi et al. 2012; Stevenson et al. 2012; Weare 2013), despite the fact that ENSO performances in the CMIP5 CGCMs have been significantly improved from those of CMIP3 (Kug et al. 2012; Kim and Yu 2012; Guilyardi et al. 2012; Bellenger et al. 2014). Several studies showed that the frequency of the central Pacific–type ENSO might increase in a warmer climate (Yeh et al. 2009; Kim and Yu 2012). Nonetheless, changes in ENSO variability in response to global warming are expected and can lead to changes in tropical–extratropical teleconnections.

Previous studies indicate that teleconnection response to ENSO would change under global warming, mainly over the North Pacific and North American regions during boreal winter season (Meehl and Teng 2007; Kug et al. 2010; Stevenson et al. 2012). However, two important aspects have not been studied: how the CMIP5 CGCMs capture the two dominant teleconnection patterns during boreal summer in their historical simulation and how the teleconnections would change under anthropogenic global warming. This study aims to answer these questions by analyzing two different runs of the 20 CGCMs in CMIP5: the historical run under changing solar–volcanic forcing and anthropogenic influences from 1979 to 2005 and the representative concentration pathway 4.5 (RCP4.5) run from 2069 to 2098. A detailed description of the models and data used are given in section 2. Section 3 evaluates the 20 CGCMs in capturing the WPNA and CGT mode as well as mean and variance of present boreal summer climate and then selects reliable models to explore future change. Future changes in the mean and variance of boreal summer climate and the two teleconnection modes are discussed in section 4. Section 5 summarizes the results of this study.

2. Model and data

a. Models and experiments

The 20 CGCMs from CMIP5 are used in this study. Table 1 lists the model name, institution, and horizontal resolution of the atmospheric component. Two experiments are investigated. One is the historical run (i.e., the twentieth century run) from 1979 to 2005 and the other is the RCP4.5 run from 2006 to 2100. The historical run was conducted under changing conditions consistent with observations, which may include changes in atmospheric composition (including CO_2) due to anthropogenic and volcanic influences, solar forcing, emissions or concentrations of short-lived species and natural and anthropogenic aerosols or their precursors, and land use. The RCP4.5 run assumes that radiative forcing will increase and then stabilize at about 4.5 W m^{-2} after 2100 and is chosen as a ''central'' scenario in CMIP5 (Taylor et al. 2012). Detailed information on the CMIP5 models and experiments are available online (at http://cmip-pcmdi.llnl.gov/cmip5/experiment_design.html) and in other related papers (e.g., Taylor et al. 2012).

In general, the CMIP5 CGCMs have a larger number of ensemble simulations for the historical run than for the RCP4.5 run. For a more fair comparison, we use the same number of ensemble members for the two runs in individual models. Table 1 shows the number of ensemble members used for each model. If there are more than one ensemble member in individual model experiment, we make ensemble mean before applying any analysis. To validate the CGCMs in their historical simulations with respect to observation, model data were interpolated to the common 2.5° latitude × 2.5° longitude grid. Analysis of the present climate is applied to a period from 1979 to 2008. Thus, we use historical simulation from 1979 to 2005 combined with the RCP4.5 simulation from 2006 to 2008 for models. Analysis of the future climate is applied to a 30-yr period of 2069–98.

b. Observations

The observation data used for the period 1979–2008 are as follows: 1) the National Centers for Environmental Prediction (NCEP)–U.S. Department of Energy (DOE) reanalysis II data (Kanamitsu et al. 2002) for Z200 and 200-hPa zonal wind (U200); 2) the Climate Prediction Center (CPC) Merged Analysis of Precipitation (CMAP) dataset (Xie and Arkin 1997) and Global Precipitation Climatology Project (GPCP) data version 2.2 (Huffman et al. 2009) for precipitation; and 3) the improved extended reconstructed sea surface temperature (SST) version 2 (ERSST V2) data (Smith and Reynolds 2004) for SST. All observed data were interpolated to a 2.5° latitude × 2.5° longitude grid. Like the model data, the observed climatology was obtained for the 30-yr period of 1979–2008. As a basic reference for precipitation, the merged CMAP and GPCP precipitation is used, where the two datasets are arithmetically averaged. We note that the difference between

TABLE 1. Description of CMIP5 models used in the study. Models in boldface are the six best models selected based on reproducibility of global monsoon precipitation during the historical run period, 1979–2008 (for detailed information, refer to http://cmip-pcmdi.llnl.gov/cmip5/availability.html).

Model No.	Coupled model	Expanded model name	Institution	AGCM resolution	Ensemble No.
1	ACCESS1.0	Australian Community Climate and Earth System Simulator, version 1.0	Commonwealth Scientific and Industrial Research Organization (CSIRO) and Bureau of Meteorology (BOM)	1.875° × 1.25°	1
2	BCC-CSM1.1	Beijing Climate Center, Climate System Model, 1-1	Beijing Climate Center, China Meteorological Administration	2.8125° × 2.8125°	1
3	CanESM2	Canadian Earth System Model, version 2	Canadian Centre for Climate Modelling and Analysis (CCCma)	2.8125° × 2.8125°	5
4	**CCSM4**	Community Climate System Model, version 4	National Center for Atmospheric Research (NCAR)	1.25° × 0.9375°	1
5	CNRM-CM5	Centre National de Recherches Météorologiques Coupled Global Climate Model, version 5	Centre National de Recherches Meteorologiques (CNRM)/ Centre European de Recherche et Formation Avancees en Calcul Scientifique (CERFACS)	1.40625° × 11.40625°	1
6	CSIRO Mk3.6.0	Commonwealth Scientific and Industrial Research Organisation Mark, version 3.6.0	CSIRO and the Queensland Climate Change Centre of Excellence (QCCCE)	1.875° × 1.875°	3
7	FGOALS-g2	Flexible Global Ocean–Atmosphere–Land System Model gridpoint, version 2	State Key Laboratory of Numerical Modeling for Atmospheric Sciences and Geophysical Fluid Dynamics (LASG), Institute of Atmospheric Physics, Chinese Academy of Sciences; Center for Earth System Science (CESS), Tsinghua University	2.8125° × 2.8125°	1
8	**GFDL CM3**	Geophysical Fluid Dynamics Laboratory Climate Model, version 3	National Oceanic and Atmospheric Administration (NOAA)/Geophysical Fluid Dynamics Laboratory (GFDL)	2.5° × 2°	1
9	GFDL-ESM2M	Geophysical Fluid Dynamics Laboratory Earth System Model 2M		2.5° × 2°	1
10	GISS-E2-R	Goddard Institute for Space Studies Model E2, coupled with the Russell ocean model	National Aeronautics and Space Administration (NASA) Goddard Institute for Space Studies (GISS)	2.5° × 2°	2
11	HadGEM2-CC	Hadley Centre Global Environment Model, version 2—Carbon Cycle	Met Office Hadley Centre (MOHC)	1.875° × 1.24°	1
12	**HadGEM2-ES**	Hadley Centre Global Environment Model, version 2—Earth System		1.875° × 1.24°	1
13	INM-CM4.0	Institute of Numerical Mathematics Coupled Model, version 4	Institute of Numerical Mathematics (INM)	2° × 1.5°	1
14	IPSL-CM5A-LR	L'Institut Pierre-Simon Laplace Coupled Model, version 5A, coupled with Nucleus for European Modelling of the Ocean (NEMO), low resolution	L'Institute Pierre-Simon Laplace (IPSL)	3.75° × 1.875°	4
15	**IPSL-CM5A-MR**	L'Institut Pierre-Simon Laplace Coupled Model, version 5A, coupled with NEMO, mid resolution		2.5° × 1.258°	

TABLE 1. (*Continued*)

Model No.	Coupled model	Expanded model name	Institution	AGCM resolution	Ensemble No.
16	**MIROC5**	Model for Interdisciplinary Research on Climate (MIROC), version 5	Atmosphere and Ocean Research Institute (University of Tokyo), National Institute for Environmental Studies, and Japan Agency for Marine-Earth Science and Technology (JAMSTEC)	1.40625° × 1.40625°	1
17	MIROC-ESM	MIROC, Earth System Model		2.8125° × 2.8125°	1
18	MPI-ESM-LR	Max Planck Institute Earth System Model, low resolution	Max Planck Institute for Meteorology (MPI-M)	1.875° × 1.875°	3
19	MRI-CGCM3	Meteorological Research Institute Coupled Atmosphere–Ocean General Circulation Model, version 3	Meteorological Research Institute (MRI)	1.125° × 2.25°	1
20	**NorESM1-M**	Norwegian Earth System Model, version 1 (intermediate resolution)	Norwegian Climate Centre (NCC)	2.5° × 1.875°	1

CMAP and GPCP is not significant in terms of climatology and total variance. The pattern correlation coefficient between CMAP and GPCP in June–August (JJA) is 0.95 and 0.88 for climatology and variance, respectively, over all longitudes and between 60°S and 60°N. To focus on year-to-year variations, the interannual component of the data is used to analyze variance and major modes of variability. The long-term trend and decadal variations with periods longer than 8 yr are removed using Fourier harmonic analysis of the seasonal mean JJA anomalies. The same arithmetical processes such as horizontal interpolation and the period for climatology are applied to model outputs.

c. *Construction of multimodel mean*

This study adopts the multimodel mean (MMM) approach rather than the multimodel ensemble (MME) method for analyzing interannual variability and major mode of variability in model simulations similar with the approach taken by Chu et al. (2014). This is because individual models have different characteristics on modes of variability: particularly periodicity, center of action, and amplitude of ENSO (Bellenger et al. 2014). MMM is equivalent to MME for long-term mean but not for variability. In the MME approach, variance is calculated from the anomaly of MME with the total sample size of 30; instead, however, the MMM approach averages the variances of individual models with the total sample size of 30 multiplied by the number of models used. The method used to obtain the modes of variability also differs between the two approaches. In the MME method, we first calculate mean of all models (e.g., MME) and then apply EOF analysis to anomalies of MME (e.g., Lee et al. 2011). However, in the MMM approach, we first piece together individual model's ensemble simulation normalized by its own standard deviation and then apply EOF analysis on the consecutive data. This way offers a better chance of identifying common feature of major modes of variability among models without cancellation of each model's different intrinsic mode of variability than the MME approach provides. A degree of freedom is also different. For example, sample size is 30 (the total number of year) in MME but the MMM approach uses 30 multiplied by the number of models being used at each grid point.

3. Evaluation and selection of CMIP5 CGCMs

In this section, we assess ability of simulating the two dominant teleconnection patterns during boreal summer in the 20 CMIP5 CGCMs for the 30-yr period of 1979–2008. In addition, we evaluate the models' performance on 1) variance of Z200 (0°–90°N and all longitudes), 2) long-term mean of U200 (0°–90°N and all longitudes), 3) long-term mean and variance of precipitation (30°S–60°N and all longitudes), and 4) long-term mean and variance of JJA and DJF tropical SST (30°S–30°N and all longitudes) because the models' performance for simulating seasonal mean climatology is significantly related to their performance in variability (Lee et al. 2010).

According to Ding et al. (2011), the two dominant teleconnection modes can be identified by applying either maximum covariance analysis (MCA) on the JJA NH Z200 and tropical rainfall or EOF analysis on the NH Z200. The results are almost the same between the two analyses. Lee et al. (2011) also demonstrated that the first and second EOF modes of JJA Z200 do

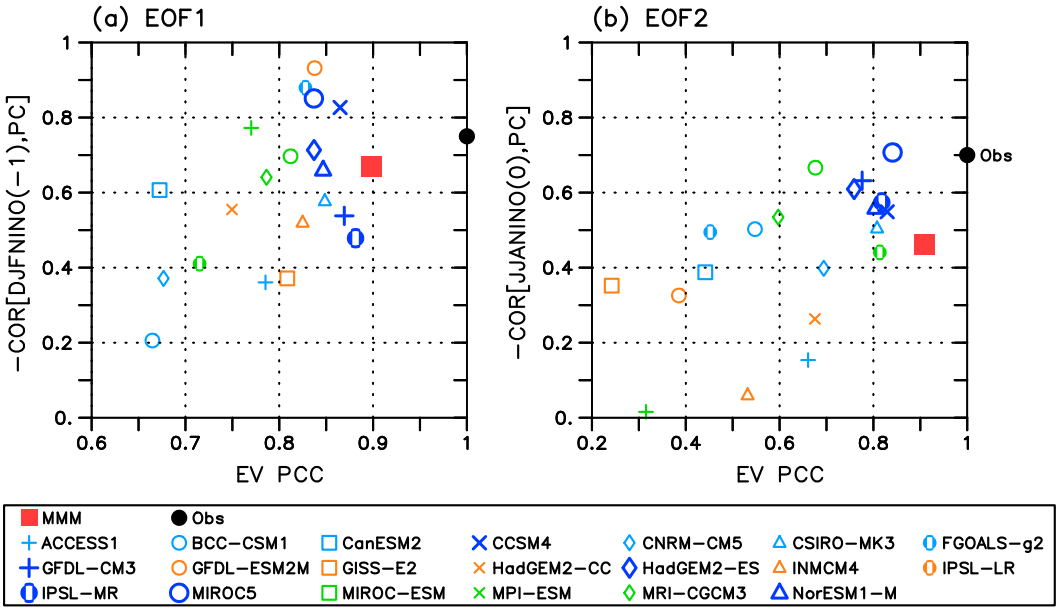

FIG. 2. Performance of the 20 CGCMs in simulating the (a) first and (b) second EOF modes of JJA Z200 anomalies over the NH in terms of the PCC between the observed and simulated eigenvector (EV) field (abscissa) and relationship with ENSO (ordinate). In (a), the correlation coefficient (COR) between the first PC and Niño-3.4 SST during the preceding DJF season multiplied by −1 is shown (the observed value is 0.75). In (b), the COR between the second PC and simultaneous Niño-3.4 SST multiplied by −1 is displayed (the observed value is 0.7). The assessment for the combined analysis of all models (MMM) is also shown. Thick blue marks denote the best six models that are selected in the section: CCSM4, GFDL CM3, HadGEM2-ES, IPSL-CM5A-MR, MIROC5, and NorESM1-M.

a good job of representing the WPNA and CGT, respectively. These modes are not only highly predictable but also statistically separable from other higher modes. This study applies the EOF analysis on interannual component (2–8-yr variability) of JJA Z200 anomalies using the correlation matrix over the NH (0°–80°N and all longitudes) in order to identify the teleconnections and evaluate the models' reproducibility of the modes. The square root of cosine of latitude weighting was used in computing the correlation matrix.

a. The WPNA mode

Figure 1 shows the observed and simulated first EOF patterns of JJA Z200 anomalies for 1979–2008. The observed first EOF mode, the WPNA, accounts for 35.0% of the total variance and is characterized by an overall zonally oriented mode of variability of negative height anomalies and positive height anomalies extending from East Asia across the entire North Pacific to western North America. The associated precipitation field shows significant positive and negative anomalies likely propagating from the WNP via East Asia and Sea of Okhotsk to northwestern and southeastern North America (Fig. 1a, top). The associated principal component (PC) time series (PC1) shows interannual variability with a major time scale of 4–5 yr. The PC1 has a significant correlation coefficient (R) with the preceding DJF Niño-3.4 SST index ($R = -0.75$), indicating that it tends to occur in the summers following ENSO peak phase. A positive phase of the WPNA tends to occur during a summer after a La Niña peak phase. The WPNA has a significant relationship with the WNPSM rainfall as well. The correlation coefficient between the PC1 and WNPSM rainfall averaged over the region 7.5°–22.5°N, 127.5°E–180° is 0.57 for the 30 yr.

Figure 1b shows the corresponding model results for EOF1. Again, EOF analysis has been applied to the consecutive data from all models in order to identify common features of the major modes of variability among models. The multimodel EOF analysis slightly underestimates the percentage variance of the WPNA compared to the observed, accounting for 30% of total variance. The pattern correlation coefficient (PCC) between the observed and simulated (by multiple models) WPNA pattern is 0.9 over the entire NH. The models also capture the relationship between the PC1 and preceding DJF Niño-3.4 SST index with a correlation coefficient of −0.67. The models reproduce the overall zonally oriented pattern over the tropics well but have difficulty in capturing the positive height anomalies

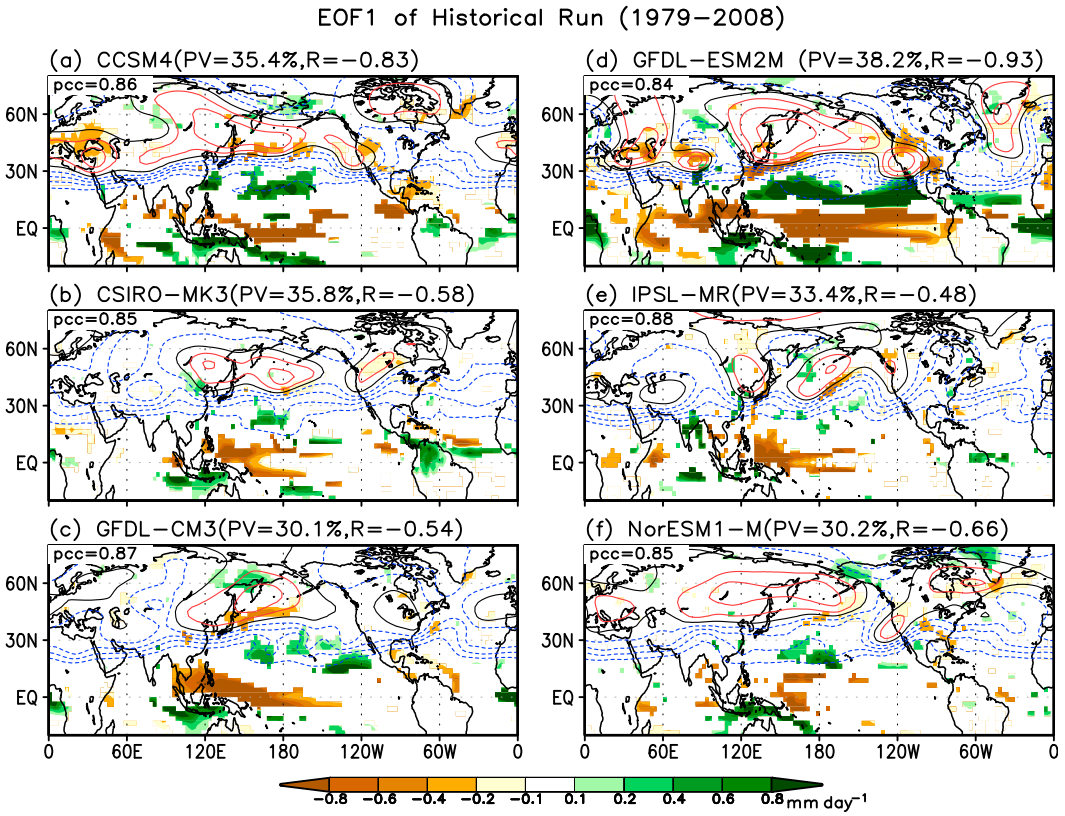

FIG. 3. Spatial patterns (contour) of the first EOF of JJA Z200 anomalies simulated by (a) CCSM4, (b) CSIRO Mk3, (c) GFDL CM3, (d) GFDL-ESM2M, (e) IPSL-CM5A-MR, and (f) NorESM1-M for the period of 1979–2008. Percentage variance (PV) and correlation (R) between the PC1 and the preceding DJF Niño-3.4 SST are also given. The numbers in the top-left corner indicate the PCC between the observed and simulated EV1. The regressed JJA precipitation anomalies against the corresponding principal component that exceed a statistical significant test at 95% confidence level are shaded.

extend from East Asia across the entire North Pacific to western North America. The models' failure in capturing the wavelike pattern may be attributed to the model's striking deficiency in simulating the associated WNPSM precipitation anomalies. While the observed WPNA has a significant correlation (0.57) with the WNPSM rainfall, the correlation coefficient between the simulated WPNA and WNPSM precipitation is 0.15 for the 20-model MMM. Among the 20 models, one model overestimates, two are realistic, and the remainder significantly underestimates the correlation. Figure 1b further shows that the models tend to underestimate the associated positive precipitation anomalies over the WNP and negative anomalies over East Asia. However, they overestimate the associated precipitation anomalies over the Maritime Continent and western equatorial Pacific. The observed positive precipitation anomalies over southern and western United States is not captured as well. Nonetheless, the WPNA mode obtained from MMM approach is much better than individual models (Fig. 2a).

Figure 2a summarizes individual model's PCC skill for capturing the spatial distribution of the WPNA and their relationship with preceding ENSO; the MMM's skill is also presented. The CMIP5 CGCMs have a certain spread of the PCC for the WPNA mode ranging from 0.66 to 0.88. The model that best captures the spatial distribution of the WPNA is IPSL-CM5A-MR, but it underestimates the relationship with preceding ENSO ($R = -0.48$). However, we note that a model that has a better PCC for the EOF1 tends to have a stronger relationship with the preceding ENSO.

Figure 3 shows the WPNA pattern simulated by the top six models selected based on the PCC skill (Fig. 2a). The selected models are CCSM4, CSIRO Mk3, GFDL CM3, GFDL-ESM2M, IPSL-CM5A-MR, and NorESM1-M. Each model has a different systematic bias, but all tend to underestimate the positive precipitation anomalies over the Philippine Sea and WNP region, which leads to significant bias in circulation and precipitation over East Asia and North America. None of models simulate the associated positive precipitation

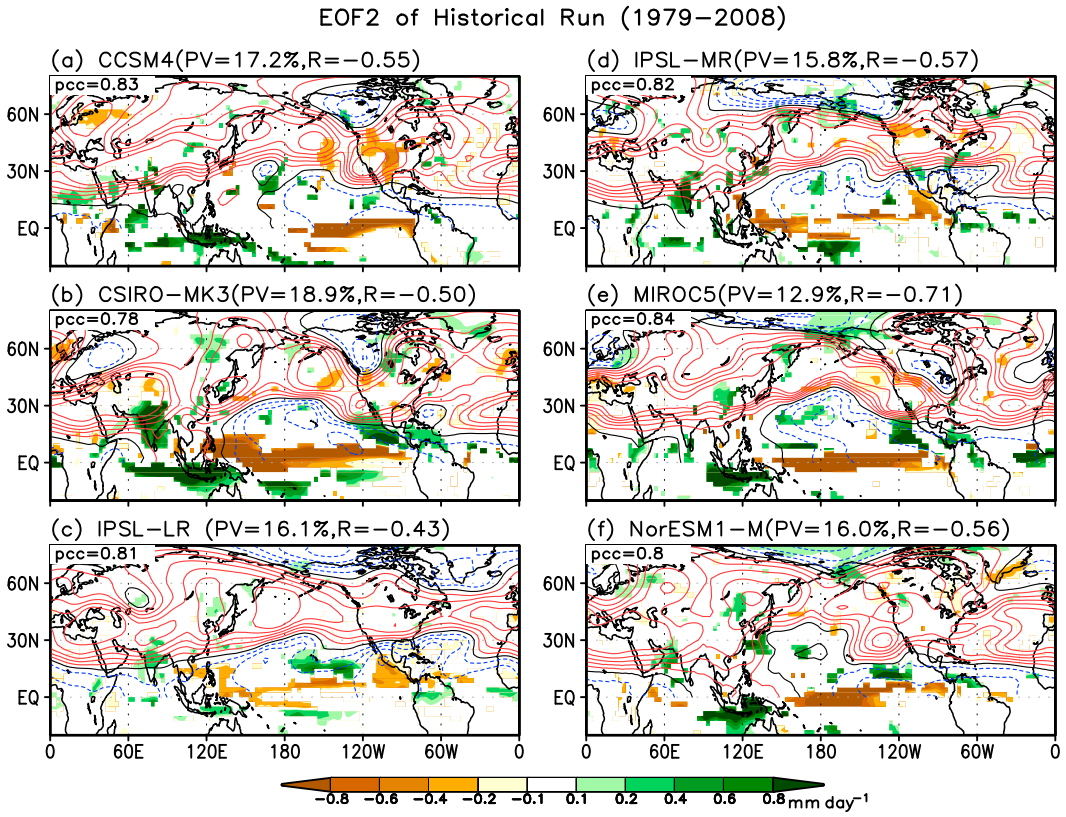

FIG. 4. As in Fig. 3, but for the second EOF simulated by (a) CCSM4, (b) CSIRO Mk3, (c) IPSL-CM5A-LR, (d) IPSL-CM5A-MR, (e) MIROC5, and (f) NorESM1-M. Here, *R* indicates the correlation coefficient between the PC2 and simultaneous JJA Niño-3.4 SST.

anomalies over the eastern part of North America. We further note that CCSM4 and GFDL-ESM2M better capture the WNP precipitation anomalies than the other models but strongly overestimate the WPNA's relationship with the preceding ENSO. The two models also overestimate the positive height anomaly and negative precipitation anomaly over the western part of North America. Thus, further improvements of coupled models are necessary for the study of the tropical and extratropical teleconnections.

To summarize, the state-of-the-art coupled models can reproduce the WPNA pattern in association with the preceding ENSO but they have a considerable deficiency in capturing the related WNPSM precipitation anomalies. This deficiency leads to the underestimation of the teleconnection pattern from the WNP via East Asia to North America.

b. The CGT mode

The second observed EOF mode representing the CGT accounts for 13.7% of the total variance and features both zonally symmetric distribution and a wavelike pattern (Fig. 1a, bottom). The zonally symmetric pattern is characterized by a positive height anomaly over the subtropics and midlatitude and by a negative height anomaly over the tropics (equatorward of 20°N). The wavelike pattern exhibits strong positive variability over southern Europe, the Mediterranean Sea, the northern part of India, the North Pacific, and the western part of North America. The spatial distribution of the regressed precipitation anomalies over the Maritime Continent and equatorial Pacific indicates that the CGT tends to occur during ENSO developing summer as discussed in Ding and Wang (2005). The correlation coefficient between the second PC (PC2) and JJA Niño-3.4 SST is −0.7, indicating that a positive phase of the CGT likely occurs during a developing La Niña summer. In addition, the positive precipitation anomalies appear over the ISM region. The correlation coefficient between the PC2 and ISM precipitation (7.5°–32.5°N, 67.5°–87.5°E) is 0.49.

The 20 models are able to reproduce the zonally symmetric distribution of the upper-level height anomalies and the associated precipitation anomalies over the ISM, WNP, the Maritime Continent, and equatorial Pacific with high fidelity as shown in Fig. 1b (bottom).

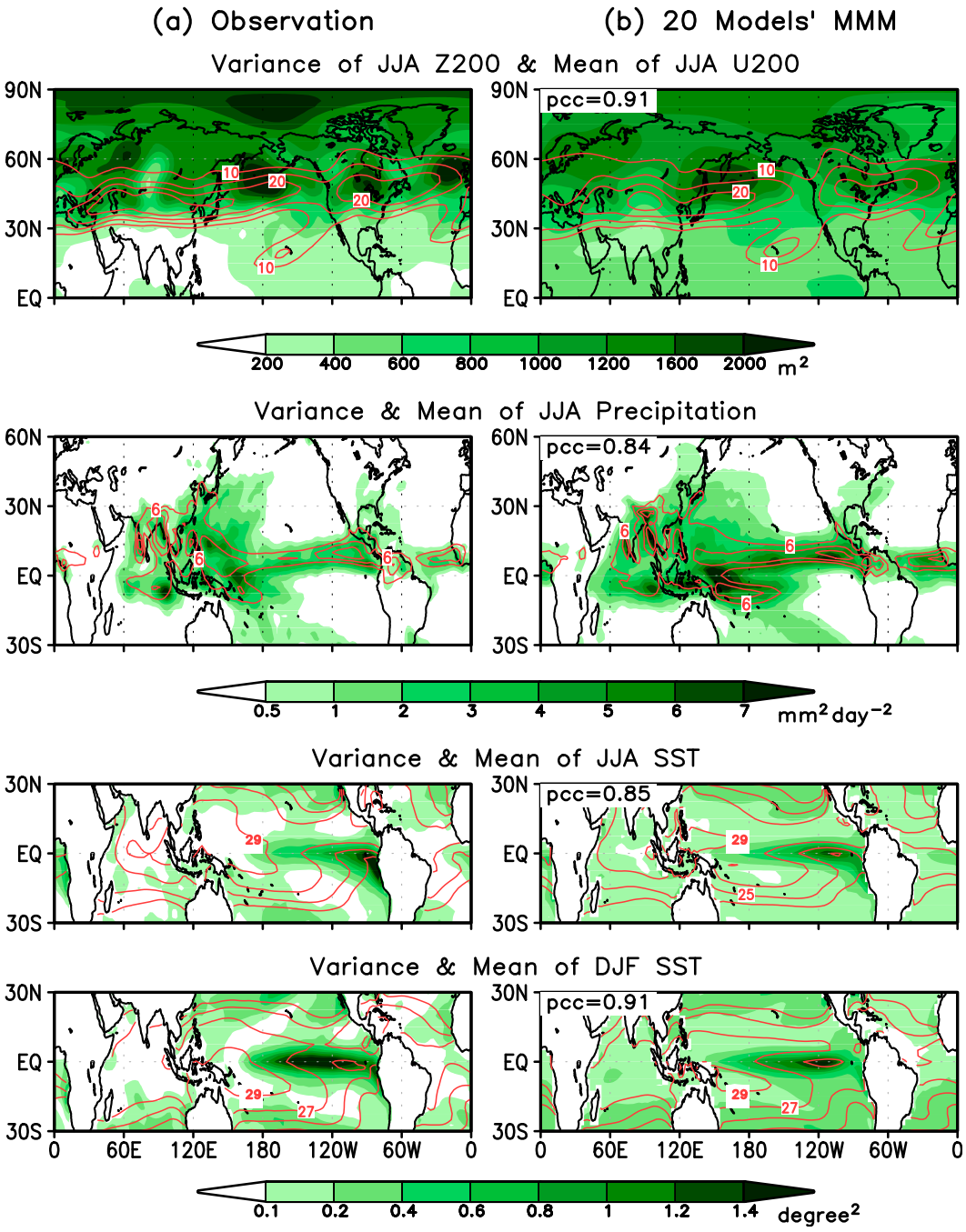

FIG. 5. Interannual variance (shading) of JJA Z200, JJA PRCP, JJA SST, and DJF SST, together with long-term mean (contour) of JJA U200, JJA PRCP, JJA SST, and DJF SST, respectively, from 1979 to 2008 obtained from (a) observations and (b) MMM of 20 CMIP5 CGCMs. Contour levels are 10, 15, 20, and 25 m s^{-1} for U200; 6, 9, and 12 mm day^{-1} for PRCP; and 21°, 23°, 25°, 27°, and 29°C for SST. For (b), individual model variances were first calculated with respect to their long-term mean and then averaged. The numbers in the top-left corners in (b) indicate the PCC between the observed and simulated variance over the entire NH for Z200; over the region 30°S–60°N at all longitudes for PRCP; and over the tropics (30°S–30°N and all longitudes) for SST.

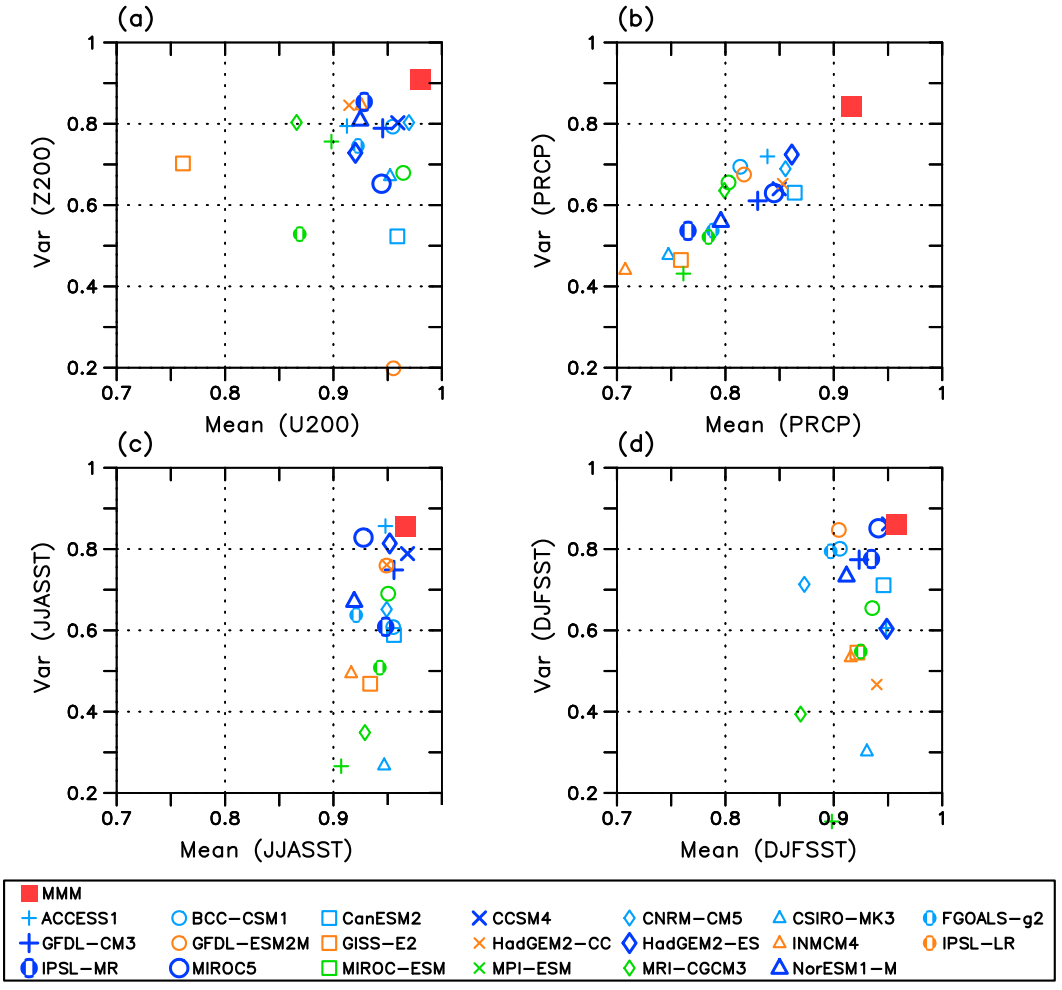

FIG. 6. Performance of 20 CGCMs in simulating (a) variance of Z200 (ordinate) and long-term mean of U200 (abscissa) and (b) variance (ordinate) and long-term mean (abscissa) of PRCP for 1979–2008 in terms of the PCC over the NH for Z200 and U200 and over the region 30°S–60°N at all longitudes for PRCP.

The models also capture some parts of the observed wavelike pattern over East Asia, the North Pacific, and North America but underestimate it over Europe and central Asia. The models also underestimate the fractional variance (11.7%) and its association with the developing ENSO. The correlation coefficient between the simulated PC2 and the simulated JJA Niño-3.4 SST is −0.45. It is interesting to note that the models are capable of capturing the CGT's association with the ISM precipitation anomaly although they tend to undervalue its relationship with the developing ENSO. The correlation coefficient between the PC2 and the ISM precipitation is 0.44 for the 20-model MMM. More than half of 20 models have realistic correlations.

The individual models have more difficulties in capturing the spatial distribution of CGT than that of WPNA, although the MMM approach has a comparable skill for the two modes (Fig. 2). Figure 2b shows that the 20 CGCMs have a considerably large spread of PCC skill for the CGT, ranging from 0.24 to 0.84. The model with a better PCC for the CGT tends to have a stronger relationship with the developing ENSO, but the models generally underestimate their relationship with ENSO, except for MIROC5, MPI-ESM, GFDL CM3, and HadGEM2-ES.

Figure 4 shows the six best models that have better PCC skill for the second eigenvector: CCSM4, CSIRO Mk3, IPSL-CM5A-LR, IPSL-CM5A-MR, MIROC5, and NorESM1-M. Four out of the six models are also selected as top models for the WPNA; they are CCSM4, CSIRO Mk3, IPSL-CM5A-MR, and NorESM1-M. The models indeed do a good job of simulating the zonally symmetric pattern along with the dipole pattern of precipitation anomalies over the Maritime Continent and equatorial Pacific but have a systematic bias in the wavelike pattern, particularly over East Asia and North

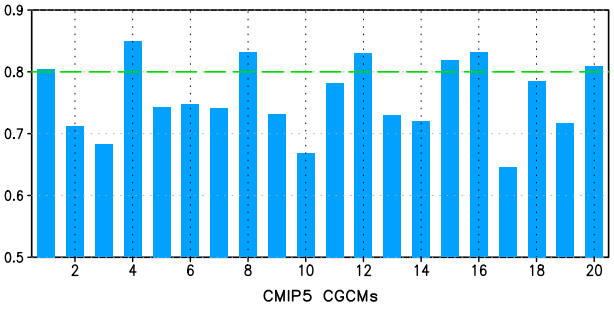

FIG. 7. The combined skill of 20 CGCMs for simulating long-term mean, interannual variance, and the first two dominant modes. See Table 1 for the corresponding model name to each model number used. The best six models exceeding the skill of 0.8 are selected.

America. The CSIRO Mk3 and IPSL models reproduce the CGT's association with the ISM precipitation anomalies well and are thus better capturing the wavelike pattern of the observed CGT compared to the other models.

To summarize, our model evaluation reveals that the current coupled models are able to reproduce the zonally symmetric patterns of the observed CGT mode, although they tend to underestimate the relationship with developing ENSO. The analysis also supports the assertion of Ding and Wang (2005) that the key factor for models to better capture the wavelike pattern of the CGT should be the realistic simulation of the associated ISM precipitation anomalies. However, further analysis and modeling experiment are necessary to better support the argument.

c. *Climatological mean and variance*

To realistically simulate tropical–extratropical teleconnections, it is important for climate models to have intrinsic modes of variability and jet stream close to the observed as also discussed by Lee et al. (2011). This section is devoted to the evaluation of the model performance in mean and total variance fields.

Figure 5 compares the observed and simulated interannual variability of upper-level circulation (Z200)

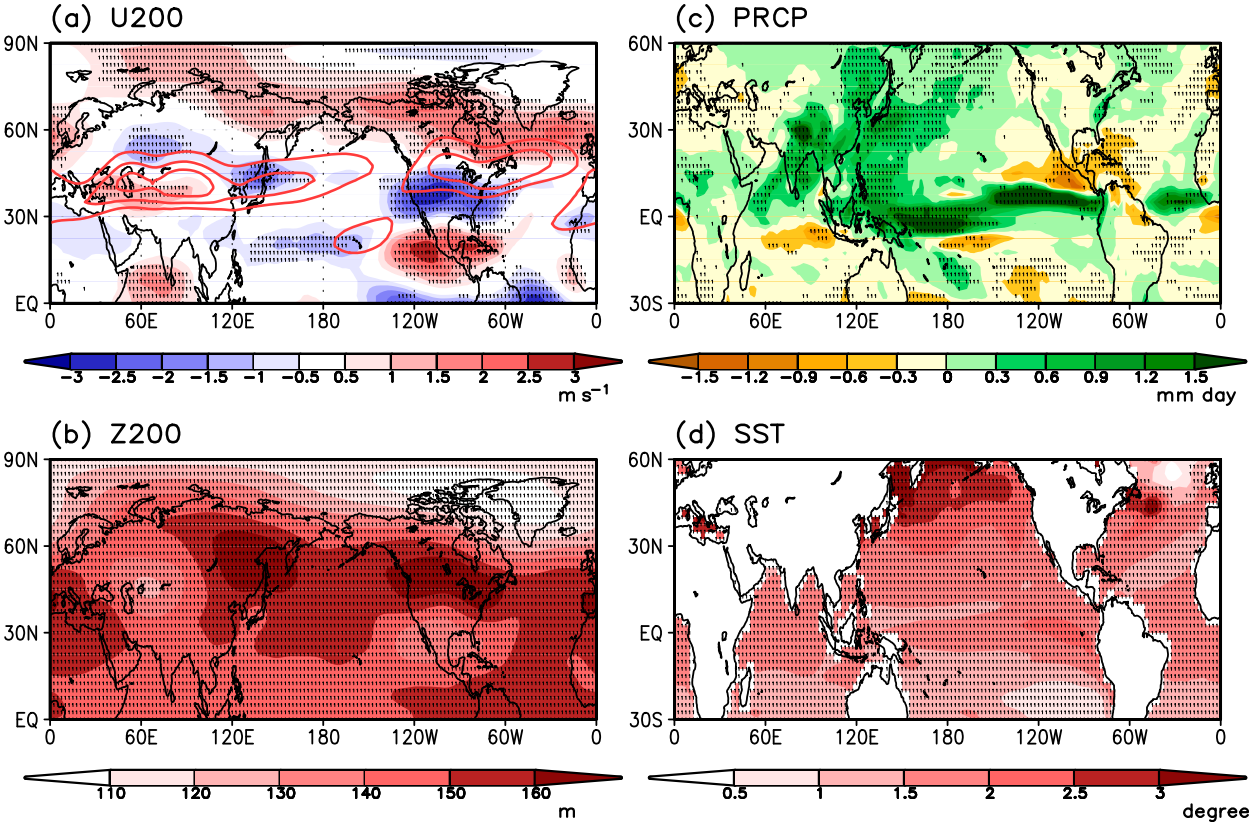

FIG. 8. Changes in the long-term climatology of JJA (a) U200, (b) Z200, (c) PRCP, and (d) SST for the B6MMM of RCP4.5 simulations for the period 2069–98 relative to those of historical simulations for the period 1979–2008 in CMIP5. Stippling denotes areas where the magnitude of the B6MMM exceeds the standard deviation of intermodel spread. In (a), the JJA climatology of U200 in the historical run (contour) is superimposed. The contour levels are 15, 20, and 25 m s^{-1}.

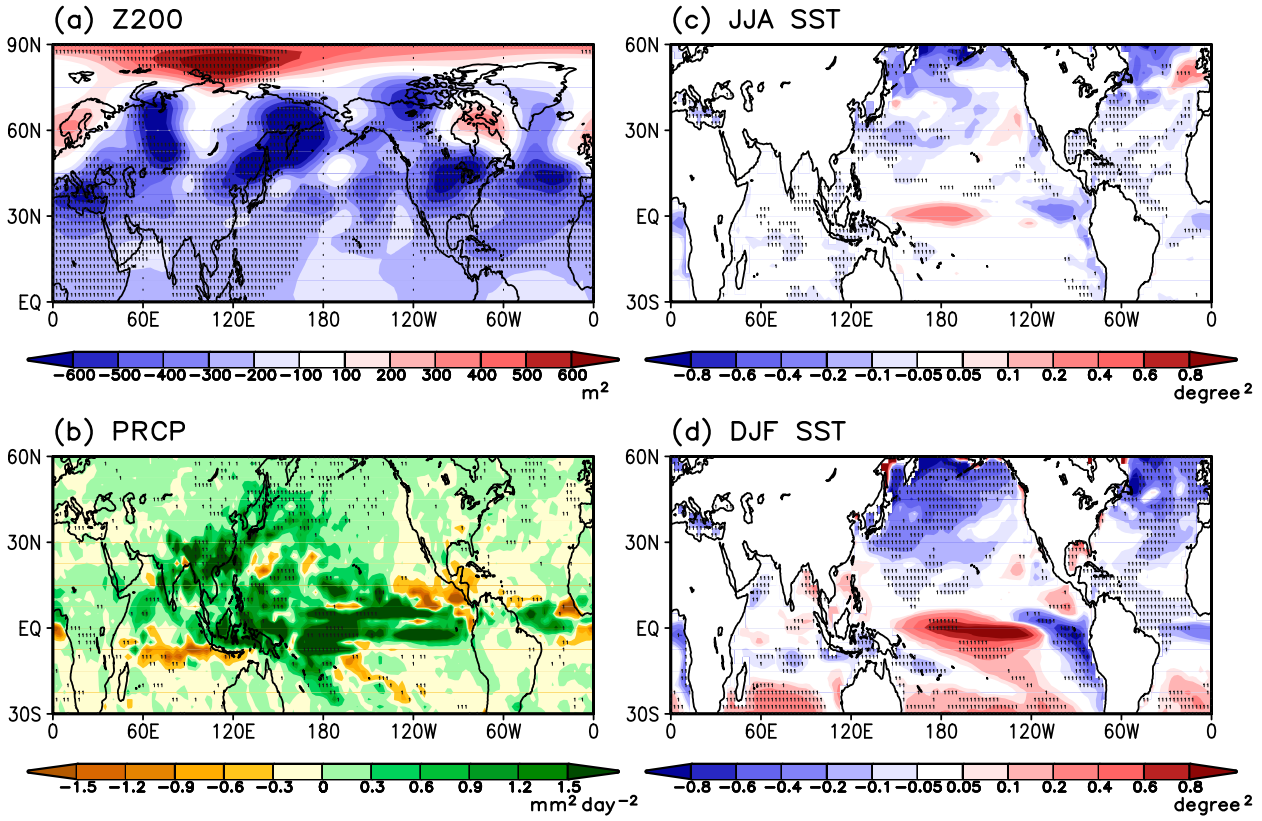

FIG. 9. As in Fig. 8, but for the variance of JJA anomalies. Before calculating future change, the variance of B6MMM is obtained by averaging the six individual model variances for each period.

along with the climatological jet stream in JJA. As described in section 2c, we combined all the models' data by averaging the variance of individual models (MMM approach). In the observation, variance is prominent in the jet exit regions over the North Atlantic and North Pacific. In the individual models, the major centers of variability and the location of jet streams are all different (not shown). However, the MMM has realistic interannual variability and jet stream due to the cancellation of inherent systematic biases of individual models. It also captures the observed major variability centers over the northeast Atlantic Ocean, Western Europe, the North Pacific, and northern North America well. The PCC between the observed and MMM's interannual variance over the entire NH amounts to 0.91.

As mentioned previously, the WNPSM and ISM rainfall play important roles for the WPNA and CGT, respectively (Ding et al. 2011). Thus, it is important for climate models to realistically simulate the mean and variance of boreal summer rainfall, particularly over the Asian monsoon region. Figure 5b shows that the MMM is capable of reproducing the climatological distribution of summer rainfall and major centers of variability over the tropics. However, the MMM tends to overestimate variability over the equatorial western Pacific and to significantly underestimate it over the Philippine Sea and the subtropical WNP. The underestimation of the mean and variance of the WNPSM precipitation is likely related to the model's failure to capture the WPNA's association with the WNPSM rainfall anomaly discussed in section 3a.

Ding et al. (2011) and Lee et al. (2011) demonstrated that the sources of the CGT and WPNA can be understood in terms of ENSO teleconnection dynamics. Thus, models' ability in capturing mean and variance of the tropical SST should be one of key factors for better simulation of the two modes. Figure 5 indicates that the state-of-the-art coupled models tend to have cold bias and weaker SST variability along equatorial Pacific as mentioned in many previous studies (e.g., Guilyardi 2006; Bellenger et al. 2014).

Figure 6 summarizes the performance of the 20 CGCMs in reproducing variance of Z200, mean of U200, and variance and mean of precipitation and SST in terms of the PCC between the observation and model simulation. The CMIP5 CGCMs show a large spread in performance, with PCC ranging from 0.53 to

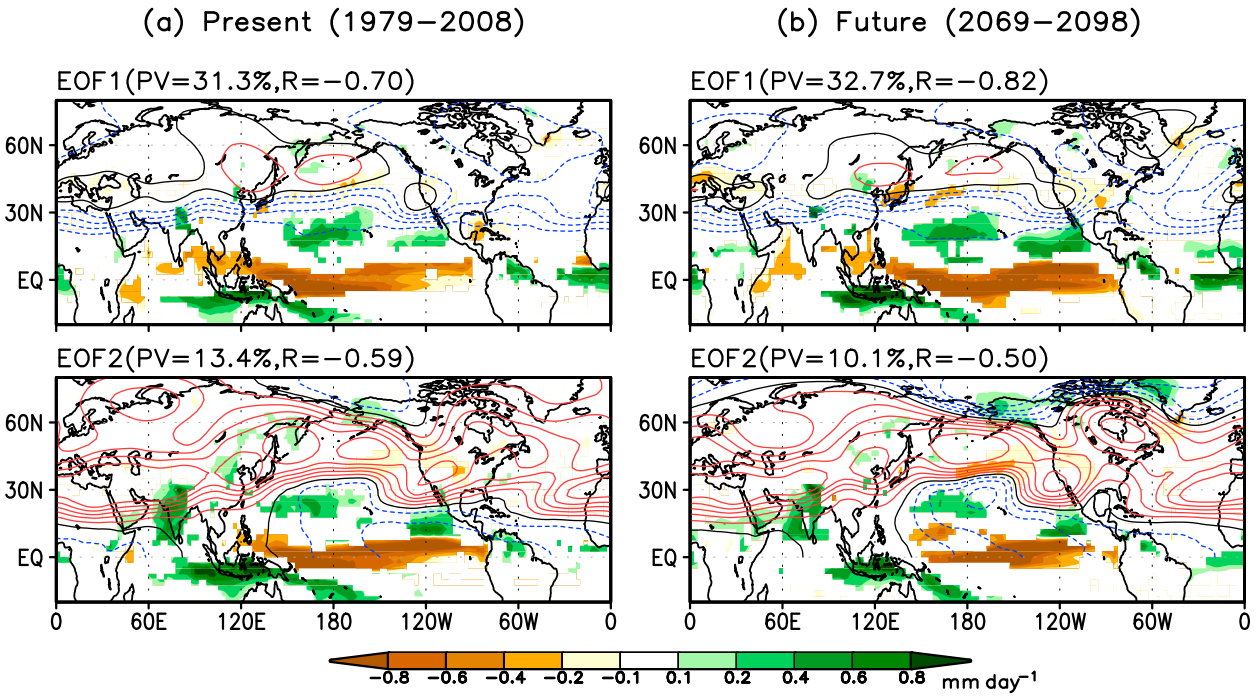

FIG. 10. Spatial patterns (contour) of the (top) first and (bottom) second EOF modes of JJA Z200 anomalies over the NH for (a) the present and (b) the future obtained from combined analysis of the select best six models. Correlation coefficients between the PC and simultaneous JJA precipitation that exceed a statistical significance test at 95% confidence level are shaded. The total sample size for the correlation is 180. PV and *R* are given (top) between the PC1 and the preceding DJF Niño-3.4 SST and (bottom) between the PC2 and the simultaneous JJA Niño-3.4 SST.

0.85 for the variance of Z200, from 0.43 to 0.72 for precipitation, and from 0.25 to 0.85 for both JJA and DJF SST. The MMM has much better skill than individual models in all aspects. As Lee et al. (2010) indicated, the model that has a realistic simulation of the mean field tends to have better simulation of variance, particularly for precipitation. This suggests that correction of the inherent bias in the mean state of model is critical for improving the intrinsic mode of variability.

d. Selection of reliable models

Based on the 20 models' performance on mean and variance shown in Fig. 6 and on the two teleconnections shown in Fig. 2, we select reliable models from the 20 CGCMs. For the selection, a combined skill ($\text{Skill}_{\text{com}}$) is defined as follows:

$$\text{Skill}_{\text{com}} = 0.5(\text{Average of PCCs for variance and mean}) + 0.5\left(\frac{\lambda_1}{\lambda_1+\lambda_2}\text{PCC}_{\text{EV1}} + \frac{\lambda_2}{\lambda_1+\lambda_2}\text{PCC}_{\text{EV2}}\right).$$

The first term denotes the average of PCCs for variance of Z200 and climatology of U200 over the entire NH; variance and climatology of precipitation over the region 30°S–60°N at all logitudes during JJA; and variance and climatology of SST during JJA and DJF over the tropics (30°S–30°N and all longitudes) shown in Fig. 6. The second term includes the PCCs for the first and second EOF weighted by their eigenvalues of the observation, shown in Fig. 2. The observed first eigenvalue (λ_1) is 0.35 and the second one (λ_2) is 0.14.

Figure 7 shows the combined skill for each model. We select the six best models that have the combined skill exceeding 0.8. The select six models are CCSM4, GFDL CM3, HadGEM2-ES, IPSL-CM5A-MR, MIROC5, and NorESM1-M. ACCESS1 (model 1) is not chosen because it has much less skill for the two teleconnection modes compared to the select six models as shown in Fig. 2. The high combined skill of ACCESS1 mainly comes from its ability to simulate climatology and total variance (Fig. 6). Inclusion or exclusion of ACCESS1 does not affect major conclusions of this study. It should be mentioned that the definition of combined skill and threshold value for the model selection is rather subjective. However, the big advantages using the six best models' MMM (B6MMM) are that 1) it has better skills for the two teleconnection modes as well as mean and variance and 2) it contains less

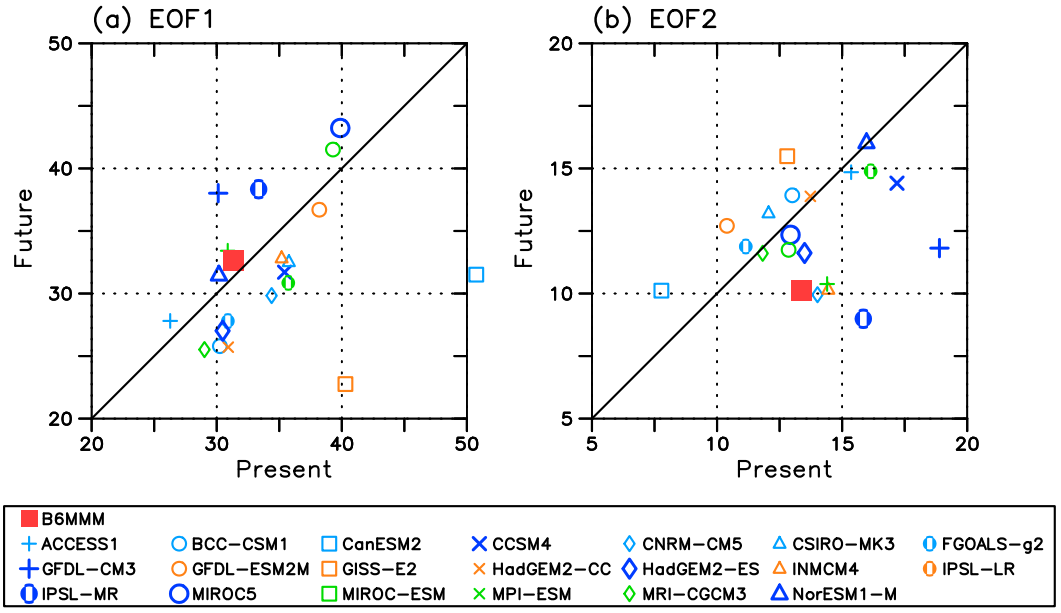

FIG. 11. Scatter diagram of PV of the (a) first and (b) second EOF for the present period of 1979–2008 (abscissa) vs the future period of 2069–98 (ordinate) simulated by 20 CGCMs. The marks for the best six models are larger than those for the other models. Results of B6MMM are also given with red closed squares. The diagonal line indicates that PV for the future is equal to that of the present.

uncertainty (i.e., intermodel spread against MMM) compared to all the models' MMM.

To identify the two teleconnection modes in the B6MMM, we apply EOF analysis on the six selected models after normalizing each model datum by its own standard deviation. The total sample size for the analysis is 180 [the total number of years (30) multiplied by 6]. We found that the B6MMM have better PCCs for the first and second EOFs and its ENSO relationship is closer to the observed than individual models as well as the 20-model MMM. The PCC for the B6MMM is 0.9 for the WPNA and 0.91 for the CGT. The correlation with ENSO in the B6MMM (20-model MMM) is −0.7 (0.67) for the WPNA and −0.59 (0.48) for the CGT.

4. Future changes in mean, variance, and teleconnections

a. *Mean and variance*

Before investigating changes in the teleconnections, this section discusses future changes in the mean and variance of Z200, U200, precipitation, and SST during boreal summer by comparing the historical (1979–2008) and the RCP4.5 (2069–98) simulation using the best six models selected in section 3d.

Figure 8 shows changes of the JJA climatology of U200, Z200, precipitation, and SST projected by the B6MMM. Stippling indicates an area where the magnitude of the change exceeds the uncertainty measured by the standard deviation of intermodel spread against the B6MMM. The B6MMM projects significant warming all over the NH at the upper level as well as on the surface as shown in Figs. 8b,d. The warming is much larger over the extratropical NH between 25° and 70°N. Lee and Wang (2014) and Xiang et al. (2014) demonstrated that the CMIP5 models project larger warming in the upper troposphere than lower troposphere, indicating atmospheric stabilization. The upper-level jet, which is associated with latitudinal differential warming, is expected to weaken over East Asia and the North Pacific and to shift significantly northward over the North America and North Atlantic (Fig. 8a). However, the jet over Southern Europe and central Asia is projected to shift southward. Although the atmospheric stabilization happens, JJA precipitation will significantly increase over the NH, particularly over the Asian summer monsoon (ASM) region and equatorial Pacific, as demonstrated by Lee and Wang (2014), Wang et al. (2014), and Seo et al. (2013). Nonetheless, it is important to mention that the CMIP5 models' projection for future monsoon change may be highly uncertain since the ASM precipitation is the most difficult element for numerical models to simulate and predict (Wang et al. 2009; Lee et al. 2010).

Figure 9a indicates that the warming in the upper troposphere and the increase in atmospheric stability will lead to a significant decrease in JJA atmospheric variability over most of the extratropical NH. On

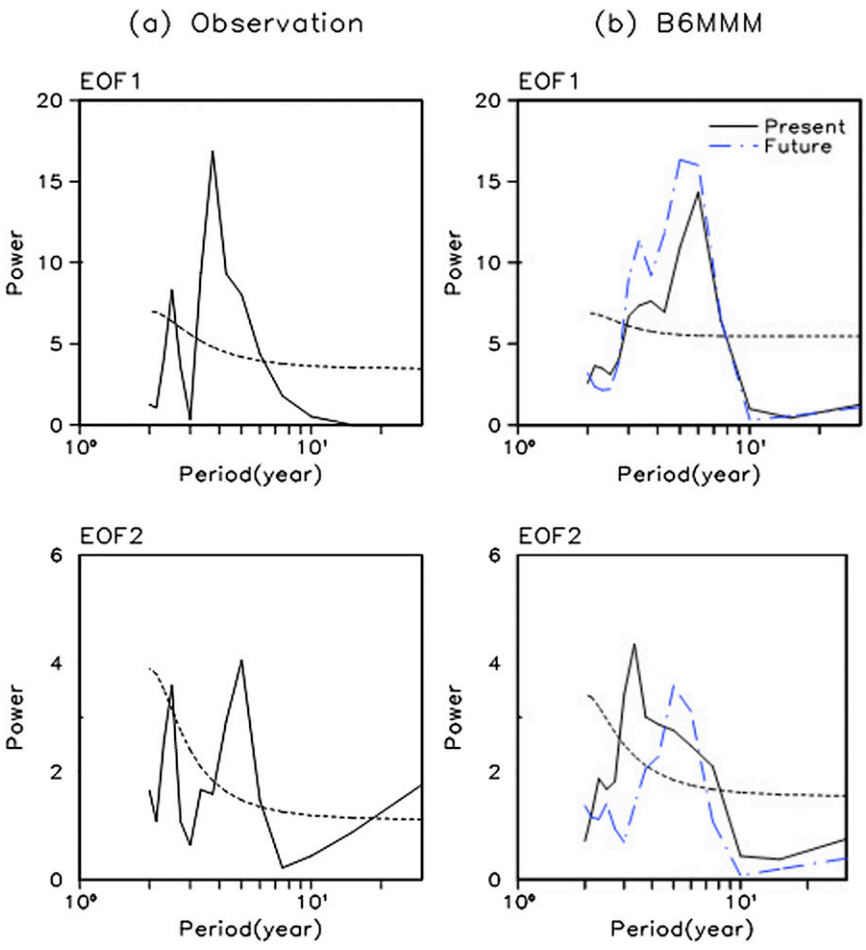

FIG. 12. The power spectral density of the (top) first and (bottom) second PC time coefficients obtained from (a) observations and (b) B6MMM. In (b), the results are obtained from averaging the power spectral density of the PCs of six best models for the present (black solid) and future (blue long dashed and dotted) periods. The black dashed line indicates red noise at 95% confidence level.

average over the entire NH, the Z200 variability is projected to decrease by 34%. The B6MMM also predicts a significant decrease in SST variability over many parts of NH oceans but a slight increase in ENSO variability during the boreal winter. However, the increases in SST variability over the western equatorial Pacific during JJA (Fig. 9c) and over the central equatorial Pacific during DJF (Fig. 9d) are smaller than the intermodel spread. JJA precipitation variability will increase significantly over the ASM and the equatorial Pacific, similar to the increase in mean precipitation attributable to enhanced atmospheric moistening. We further note that all the models' MMM projects similar changes in mean and variance of Z200, precipitation, and SST as the B6MMM. However, uncertainty in the all models' MMM is much greater because of the larger intermodel spread than the B6MMM.

b. *Teleconnections*

This section compares the WPNA and CGT modes during the present (1979–2008) and the future (2069–98) obtained from the B6MMM. Particular attention is paid to changes in their spatial distribution, percentage variance, major frequency, and relationship with ENSO under the RCP4.5 scenario.

1) THE WPNA MODE (EOF1)

As mentioned in section 3, the B6MMM can reproduce the EOF1 and EOF2 more realistically than individual models and all models' MMM to a certain extent. The PCC between the observed and B6MMM's EOF1 is 0.9 over the NH during the present period (Fig. 10a). It also better captures the associated precipitation (PRCP) pattern, although it still tends to

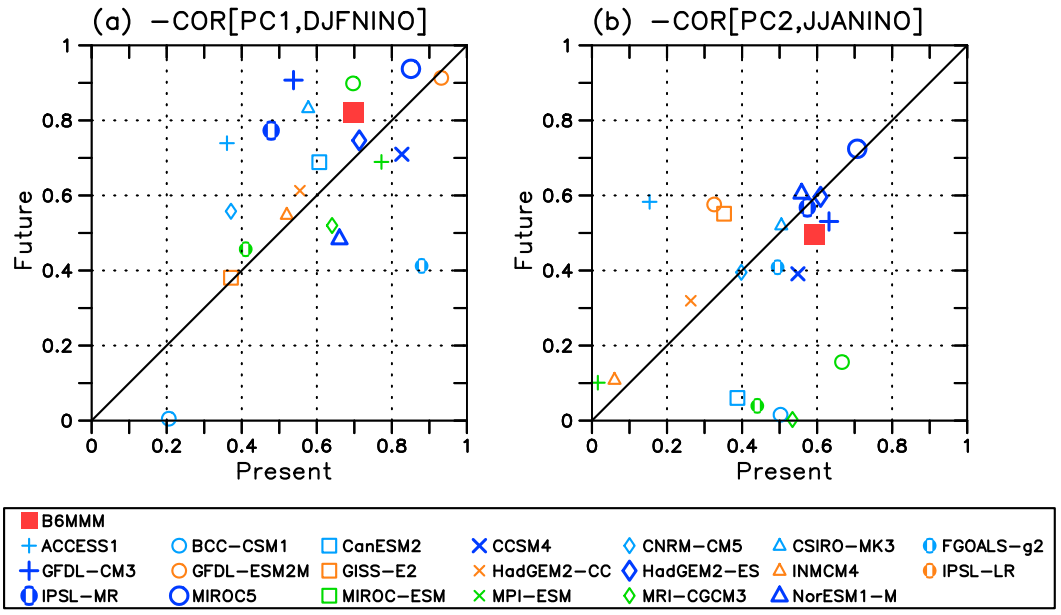

FIG. 13. Scatter diagram of COR (a) between the PC1 and the preceding DJF Niño-3.4 SST and (b) between the PC2 and simultaneous JJA Niño-3.4 SST for the present (abscissa) vs the future (ordinate) simulated by 20 CGCMs. For convenience, the correlation value is multiplied by −1. The marks for the best six models are larger than those for other models. Results of B6MMM are also given with a red closed square. The diagonal line indicates that the PV for the future is equal to that of the present.

underestimate the positive correlation over the WNP and negative correlation over East Asia but overestimate the relationship over the Maritime Continent, western equatorial Pacific, and Southern Europe (shown in Fig. 10a). The observed positive correlation over southern and western United States is not captured.

The B6MMM projects intensification of the WPNA mode under anthropogenic global warming in several aspects. First, the percentage variance will slightly increase from 31.3% to 32.7% in the B6MMM. Four of the best six models also predict an increase in the percentage variance shown in Fig. 11a. However, it should be noted that the total variance of the PC1 will decrease significantly because of the reduction of the total atmospheric variability although the contribution of the WPNA to total variability will slightly increase. Second, the teleconnection and its correlation with PRCP will strengthen particularly over the eastern Pacific–North America and the North Atlantic–Europe. Third, interannual variability with 2–4 and 5–6-yr time scales will be significantly enhanced (Fig. 12). Figure 12 shows the power spectrum density distribution and corresponding background red noise of the observed and B6MMM's PC1. The red noise curve is derived from the first order of the autoregressive process with a significance level of 0.05. In the observation (B6MMM), the WPNA mode has a major spectral peak at 4 (5–6) yr and a minor peak around 2–3 (3–4) yr in the present period. That is, the CMIP5 models tend to have an interannual variability of the first mode with a slightly longer time scale than the observation. The B6MMM predicts a significant increase in the power spectrum density at both spectral peaks in the future. Fourth, the relationship between the PC1 and preceding ENSO will be strengthened. The correlation between the PC1 and the preceding DJF Niño-3.4 SST index in the B6MMM is −0.7 in the present but −0.82 in the future. In addition, 4 of the best 6 models and 13 of the 20 CMIP5 models project to increase the correlation, as shown in Fig. 13a.

The enhancement of the WPNA mode in terms of global teleconnectivity, major spectral peaks, and relationship with ENSO under the anthropogenic global warming scenario in the CMIP5 models may be attributable to the strengthening of ENSO during the preceding winter. Although the increase in SST variability along the equatorial Pacific is not significant with respect to intermodel spread (Fig. 9d), a significant increase in the power spectral density in the DJF Niño-3.4 SST is expected over the range of around 2–4 and 5–6 yr (Fig. 14b, top). Figure 15a also indicates that the correlation between the PC1 and SST during preceding winter over the entire tropical Pacific and Indian Ocean will be intensified in the latter half of the twenty-first century. Chu et al. (2014) showed that the relationship between the ENSO and Indian Ocean basinwide warming (IOBW) may be enhanced in a warmer climate particularly on a quasi-biennial time

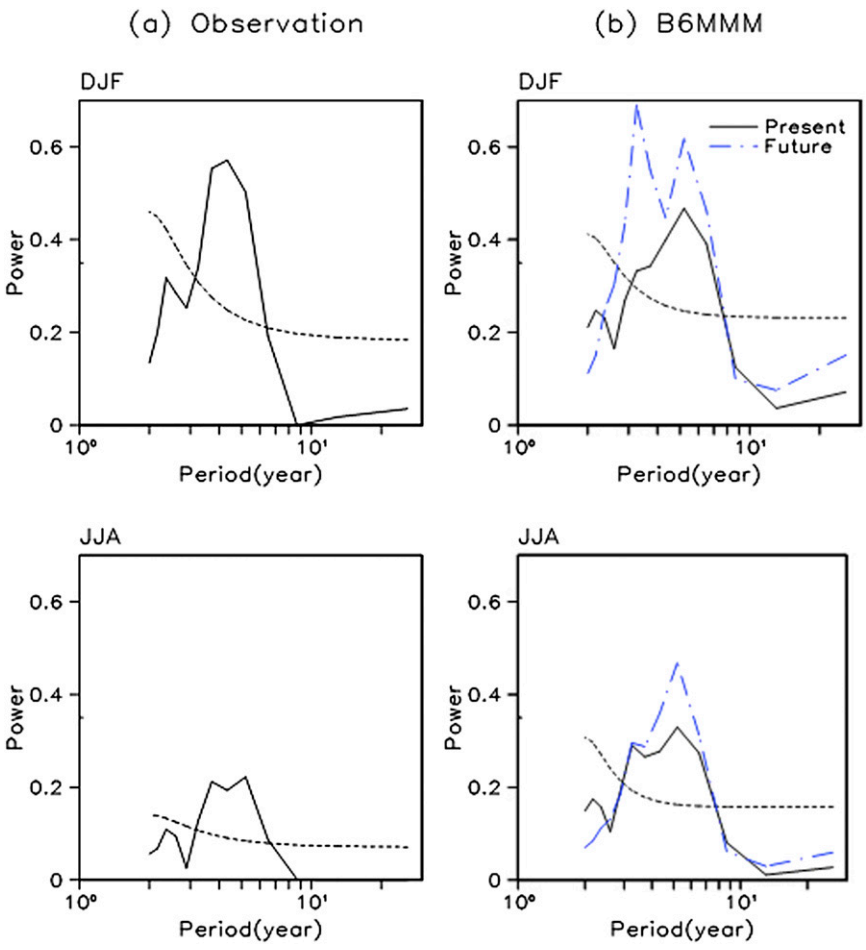

FIG. 14. As in Fig. 12, but for the (top) DJF and (bottom) JJA Niño-3.4 SST anomalies.

scale that may contribute to enhancing the WPNA mode. It is important to note that, although the WNPSM rainfall anomalies play the most important role in the WPNA mode in the observation and are not entirely linked to ENSO decay (Wang et al. 2013), the state-of-the-art models cannot reproduce the WNPSM's contribution to the WPNA change. The projected change in the relationship between the PC1 and WNPSM rainfall by the B6MMM is not large (Fig. 16a), likely because of the model's inability to reproduce the WNPSM rainfall variability. Thus, it should be mentioned that the WPNA projection by the current models needs to be considered with limited credibility.

2) THE CGT MODE

In contrast to the changes in the WPNA mode, the B6MMM tends to predict weakening of the CGT mode in many aspects. First, the percentage variance will decrease from 13.4% in the present to 10.1% in the future. The decrease (3.3%) is larger than one standard deviation error (2.8%) of the eigenvalue due to sampling estimated by the method of North et al. (1982). Figure 11b indicates that five of the best six models and more than half of the 20 CGCMs tend to predict a decrease in the percentage variance of the CGT mode. It is also noted that the reduction of the total variance of the PC2 will be significantly larger since the total variance of Z200 will decrease by 34%. Second, the NH teleconnectivity associated with the CGT may weaken over the Eastern Hemisphere but strengthen over the Western Hemisphere (Fig. 10b). In particular, the correlation of PC2 with ISM is anticipated to decrease slightly in the future (Figs. 10b, 16b). Figure 16b indicates that five out of the six best models project the significant reduction of the correlation between PC2 and ISM. Third, the major peak of the CGT variability will weaken and shift toward a lower frequency from 3–4 to 5–6 yr, as shown in Fig. 12b. Fourth, the correlation between the PC2 and the simultaneous JJA Niño-3.4 in the B6MMM will

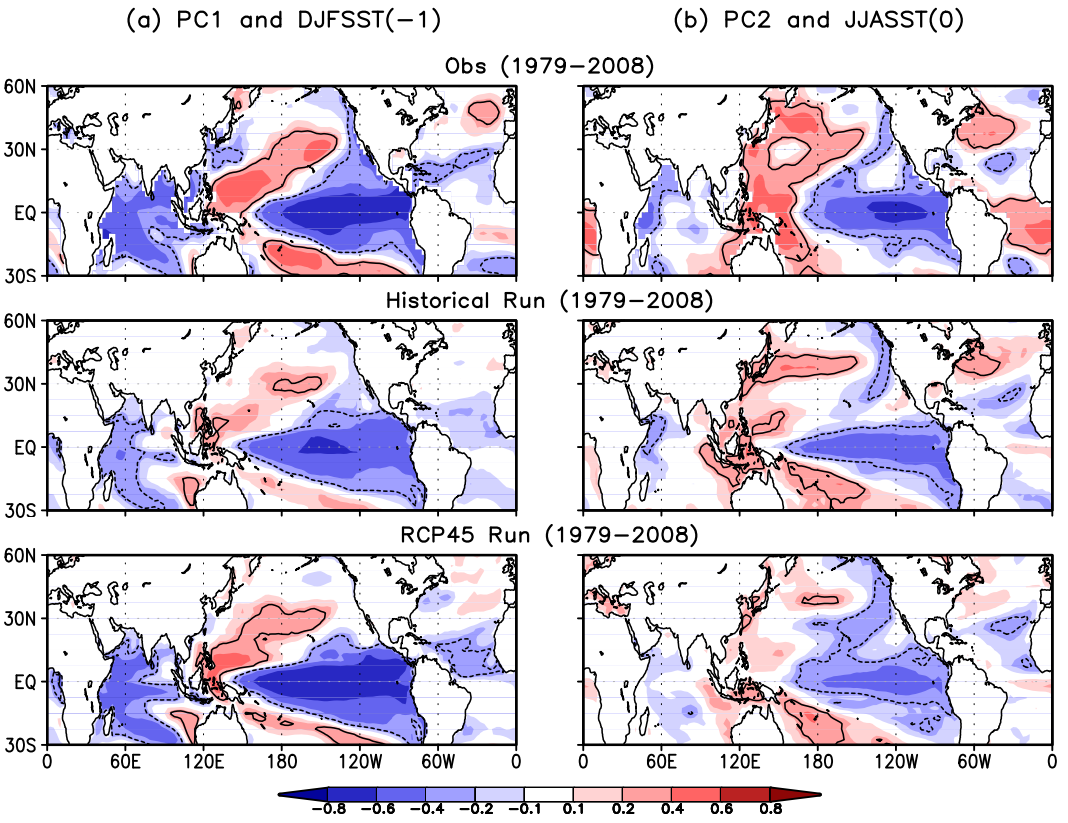

FIG. 15. The correlation coefficients between (a) the PC1 and SST anomaly during preceding boreal winter and (b) the PC2 and simultaneous SST anomaly obtained (top) from observations and from B6MMM in (middle) the historical run and (bottom) the RCP4.5 run. Correlation coefficients that exceed a statistical significant test at 95% confidence level for 30 sample sizes are contoured.

weaken from −0.59 in the present to −0.50 in the future. Figure 13b shows that most of CMIP5 models tend to project no change or a slight decrease in correlation.

Whereas a slight increase of JJA ENSO variability is projected, a weakening of the CGT is expected, particularly at the 5-yr time scale. However, the change is insignificant with respect to the intermodel spread. The weakening of the CGT mode is attributable to the weakening of its relationship with ISM rainfall variability, the atmospheric stability increase under the global warming, and weakening of the jet stream over East Asia. We also note that the ISM and ENSO relationship will weaken in the future. The correlation coefficient between them in the B6MMM is −0.55 in the present but −0.41 in the future. Thus, the decrease in the relationships among ISM and ENSO and CGT may lead to the weakening of the CGT mode. Wang et al. (2012) showed that the relationship of ISM with ENSO and CGT was weakened along with a decrease in the CGT mode after mid-1970s. Thus, we suggest that global warming will be favorable for the weakening of the ISM–ENSO relationship and the CGT.

5. Summary

This study investigates the future changes in the two dominant tropical–extratropical teleconnection modes during the boreal summer projected by 20 coupled models that participated in phase 5 of the Coupled Model Intercomparison Project (CMIP5). Our study compares two runs: the historical run under changing solar–volcanic forcing and anthropogenic influences from 1850–2005 and the RCP4.5 run that assumes that radiative forcing will stabilize at about 4.5 $W m^{-2}$ after 2100. We apply EOF analysis on the interannual component of JJA Z200 anomalies to identify the two teleconnections, the WPNA and CGT modes, and evaluate the models' reproducibility of the modes. The WPNA mode tends to occurs in summers following ENSO peak phases in association with WNPSM rainfall anomalies. The CGT mode preferentially appears in summers preceding the peak phase of ENSO cycle in association with the ISM rainfall anomaly.

Many of the 20 CMIP5 CGCMs are capable of capturing the observed interannual variability of upper-level

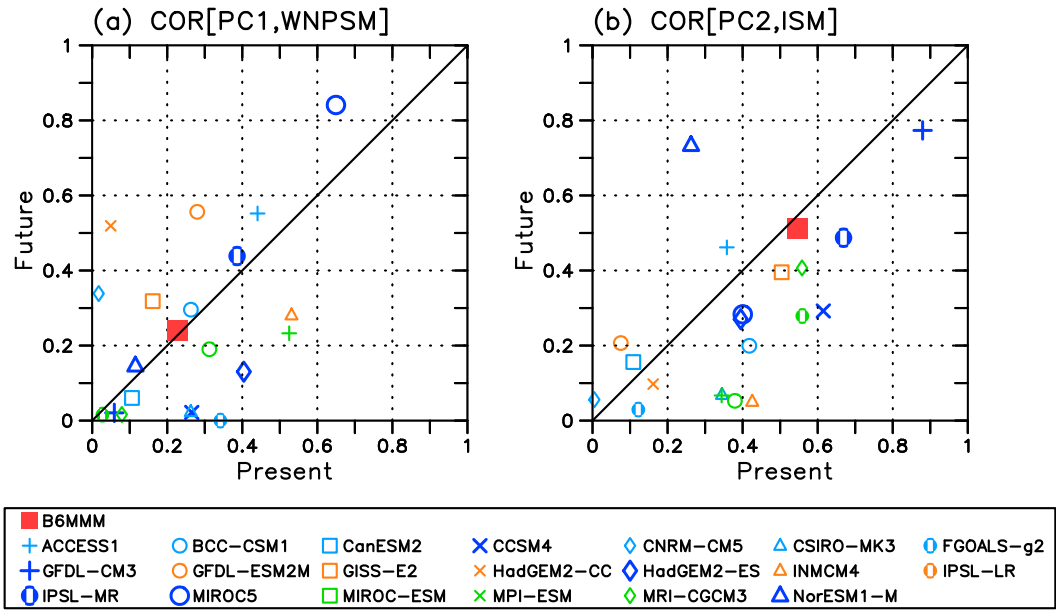

FIG. 16. Scatter diagram of COR (a) between the PC1 and WNPSM rainfall and (b) between the PC2 and ISM rainfall for the present (abscissa) vs the future (ordinate) simulated by 20 CGCMs. The results from the best six models are larger than those for other models. Results of B6MMM are also given with red closed squares. The diagonal line indicates that PV for the future is equal to that of the present.

circulation and precipitation along with a realistic reproduction of upper-level jet and mean precipitation. They can also realistically reproduce the EOF 1 mode of Z200 (WPNA) with high fidelity but with less fidelity for the EOF2 mode (CGT). The models that have realistic simulations of the mean field tend to produce better simulations of variance, particularly for precipitation. In addition, it is found that models that better capture the spatial distribution of the two teleconnection modes tend to have a stronger relationship with ENSO.

Based on the 20 models' performance on mean, variance, and the two teleconnection modes, we select a smaller number of reliable models. For the selection, a combined skill is defined using the PCC skills for mean, variance, and two teleconnection patterns. We select the six best models that have a combined skill exceeding 0.8. The six models are CCSM4, GFDL CM3, HadGEM2-ES, IPSL-CM5A-MR, MIROC5, and NorESM1-M.

The analyses of the 20 CMIP5 CGCMs and best 6 models' multimodel mean (B6MMM) reveal the following changes in the boreal summer climate and two teleconnection patterns under anthropogenic global warming (refer to Fig. 17 for schematic summary):

- Significant warming is expected over the entire NH at the upper level as well as the surface with a larger increase over the extratropics between 25° and 70°N during boreal summer. Because of the latitudinal differential warming, the upper-level jet is expected to weaken over East Asia and the North Pacific and shift significantly northward over North America and the North Atlantic.
- Interannual variance of the upper-level circulation over the entire NH extratropics will weaken because of significant atmospheric stabilization compared to the moderate increase in convective activity over most of NH regions during boreal summer.
- The WPNA mode associated with ENSO is anticipated to strengthen under anthropogenic global warming. The percentage variance will increase slightly, although the total variance of the PC1 will significantly decrease. The teleconnectivity and its relationship with PRCP will strengthen, particularly over the eastern Pacific–North America and the North Atlantic–Europe. The interannual variability with 2–4 and 5–6-yr time scales will be significantly enhanced and the relationship between the PC1 and preceding ENSO will strengthen. The enhancement of the WPNA mode in terms of global teleconnectivity, major spectral peaks, and relationship with ENSO may be attributable to the strengthening of ENSO during the preceding winter.
- The CGT mode is projected to weaken in the future. The percentage variance will decrease significantly with a considerable decrease of the PC2's total variance.

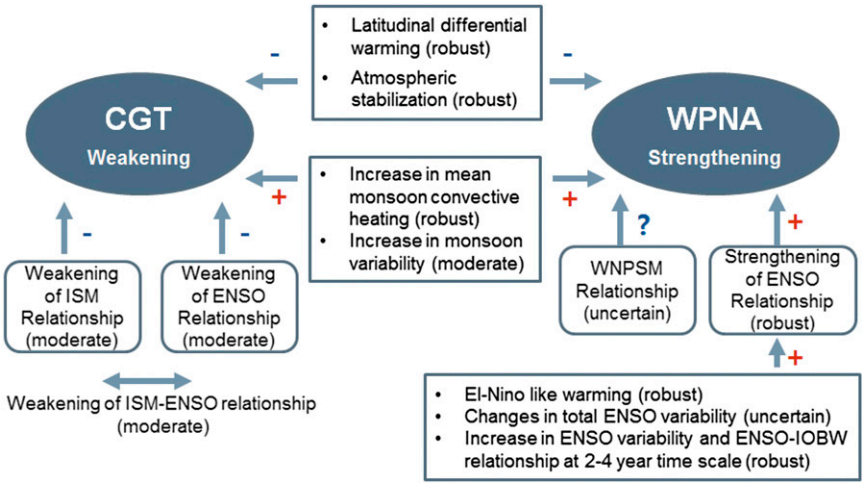

FIG. 17. Schematic showing the future changes of the CGT and WPNA under the RCP4.5 scenario projected by B6MMM. A red plus (blue minus) sign indicates positive (negative) contribution to teleconnection patterns from each component.

The NH teleconnectivity associated with the CGT will weaken over the Eastern Hemisphere but strengthen over the Western Hemisphere. The correlation of the PC2 with ISM, Southern Europe, and simultaneous JJA Niño-3.4 SST anomalies will reduce slightly in the future. The weakening of the CGT is attributable to the weakening of its relationship with ISM rainfall variability, enhanced atmospheric stability under global warming, and weakening of the relationship with developing ENSO, although boreal summer ENSO variability will not be changed much. B6MMM suggests that global warming will favor the weakening of ENSO–ISM relationship and the CGT.

This study indicates that the tropical–extratropical teleconnection characteristics would change significantly under anthropogenic global warming. These changes have important implications for future seasonal prediction because the teleconnections are significant sources of climate variability and predictability over the NH extratropics and the seasonal prediction skill for the JJA NH upper-level circulation basically comes from the coupled models' ability to properly predict the teleconnections (Lee et al. 2011). However, it is very important to mention that the future change projected by the CMIP5 CGCMs is still very uncertain because of models' poor simulation in ASM precipitation and significant bias in the tropical SST and related teleconnection characteristics.

Acknowledgments. This work was supported by the National Research Foundation of Korea (NRF) through a Global Research Laboratory (GRL) grant (MEST 2011-0021927) and IPRC, which is supported in part by JAMSTEC, NOAA, and NASA. This work was also funded by the Korea Meteorological Administration Research and Development Program under Grant CATER 2012–3071. We acknowledge the World Climate Research Programme's Working Group on Coupled Modeling, which is responsible for CMIP, and we thank the climate modeling groups listed in Table 1 of this paper for producing and making available their model output. For CMIP, the U.S. Department of Energy's Program for Climate Model Diagnosis and Intercomparison provides coordinating support and led the development of software infrastructure in partnership with the Global Organization for Earth System Science Portals.

REFERENCES

An, S.-I., and B. Wang, 2000: Interdecadal change of the structure of the ENSO mode and its impact on the ENSO frequency. *J. Climate,* **13,** 2044–2055, doi:10.1175/1520-0442(2000)013<2044:ICOTSO>2.0.CO;2.

Bellenger, H., E. Guilyardi, J. Leloup, M. Lengaigne, and J. Vialard, 2014: ENSO representation in climate models: From CMIP3 to CMIP5. *Climate Dyn.,* **42,** 1999–2018, doi:10.1007/s00382-013-1783-z.

Chu, J.-E., K.-J. Ha, J.-Y. Lee, B. Wang, B.-H. Kim, and C. E. Chul, 2014: Future change of the Indian Ocean basin-wide and dipole modes in the CMIP5. *Climate Dyn.,* doi:10.1007/s00382-013-2002-7, in press.

Collins, M., 2005: El Niño- or La Niña-like climate change? *Climate Dyn.,* **24,** 89–104, doi:10.1007/s00382-004-0478-x.

——, and Coauthors, 2010: The impact of global warming on the tropical Pacific Ocean and El Niño. *Nat. Geosci.,* **3,** 391–397, doi:10.1038/ngeo868.

Ding, Q., and B. Wang, 2005: Circumglobal teleconnection in the Northern Hemisphere summer. *J. Climate,* **18,** 3483–3505, doi:10.1175/JCLI3473.1.

——, and ——, 2007: Intraseasonal interaction between the Eurasian wave train and the Indian summer monsoon. *J. Climate,* **20,** 3751–3767, doi:10.1175/JCLI4221.1.

——, ——, J. M. Wallace, and G. Branstator, 2011: Tropical–extratropical teleconnections in boreal summer: Observed interannual variability. *J. Climate,* **24,** 1878–1896, doi:10.1175/2011JCLI3621.1.

Gu, D., and S. Philander, 1997: Interdecadal climate fluctuations that depend on exchanges between the tropics and extratropics. *Science,* **275,** 805–807, doi:10.1126/science.275.5301.805.

Guilyardi, E., 2006: El Niño–mean state–seasonal cycle interactions in a multi-model ensemble. *Climate Dyn.,* **26,** 329–348, doi:10.1007/s00382-005-0084-6.

——, and Coauthors, 2012: A first look at ENSO in CMIP5. *CLIVAR Exchanges,* No. 58, International CLIVAR Project Office, Southampton, United Kingdom, 29–32.

Ha, K.-J., J.-E. Chu, J.-Y. Lee, B. Wang, S. N. Hameed, and M. Watanabe, 2012: What causes cool summer over northern Central Asia, East Asia, and central North America during 2009? *Environ. Res. Lett.,* **7,** 044015, doi:10.1088/1748-9326/7/4/044015.

Huffman, G. J., R. F. Adler, D. T. Bolvin, and G. Gu, 2009: Improving the global precipitation record. GPCP version 2.1. *Geophys. Res. Lett.,* **36,** L17808, doi:10.1029/2009GL040000.

Jia, X., H. Lin, J.-Y. Lee, and B. Wang, 2012: Season-dependent forecast skill of the dominant atmospheric circulation patterns over the Pacific–North American region. *J. Climate,* **25,** 7248–7265, doi:10.1175/JCLI-D-11-00522.1.

——, J.-Y. Lee, H. Lin, A. Alessandri, and K.-J. Ha, 2014a: Interdecadal change in the Northern Hemisphere seasonal climate prediction: Part I. The leading forced mode of atmospheric circulation. *Climate Dyn.,* doi:10.1007/s00382-013-1988-1, in press.

——, ——, ——, H. Hendon, and K.-J. Ha, 2014b: Interdecadal change in the Northern Hemisphere seasonal climate prediction: Part II. Predictability and prediction skill. *Climate Dyn.,* doi:10.1007/s00382-014-2084-x, in press.

Kanamitsu, M., and Coauthors, 2002: NCEP dynamical seasonal forecast system 2000. *Bull. Amer. Meteor. Soc.,* **83,** 1019–1037, doi:10.1175/1520-0477(2002)083<1019:NDSFS>2.3.CO;2.

Kim, S.-T., and J.-Y. Yu, 2012: The two types of ENSO in CMIP5 models. *Geophys. Res. Lett.,* **39,** L11704, doi:10.1029/2012GL052006.

Kug, J.-S., S.-I. An, Y.-G. Ham, and I.-S. Kang, 2010: Changes in El Niño and La Niña teleconnections over North Pacific–America in the global warming simulations. *Theor. Appl. Climatol.,* **100,** 275–282, doi:10.1007/s00704-009-0183-0.

——, Y.-G. Ham, J.-Y. Lee, and F.-F. Jin, 2012: Improved simulation of two types of El Niño in CMIP5 models. *Environ. Res. Lett.,* **7,** 034002, doi:10.1088/1748-9326/7/3/034002.

Latif, M., and N. S. Keenlyside, 2009: El Niño/Southern Oscillation response to global warming. *Proc. Natl. Acad. Sci. USA,* **106,** 20 578–20 583, doi:10.1073/pnas.0710860105.

Lee, J.-Y., and B. Wang, 2012: Seasonal climate predictability of atmospheric circulation. *Climate Models,* L. M. Druyan, Ed., InTech, 19–42, doi:10.5772/33782.

——, and ——, 2014: Future change of global monsoon in the CMIP5. *Climate Dyn.,* **42,** 101–119, doi:10.1007/s00382-012-1564-0.

——, and Coauthors, 2010: How are seasonal prediction skills related to models' performance on mean state and annual cycle? *Climate Dyn.,* **35,** 267–283, doi:10.1007/s00382-010-0857-4.

——, B. Wang, Q. Ding, K.-J. Ha, J.-B. Ahn, A. Kumar, B. Stern, and O. Alves, 2011: How predictable is the Northern Hemisphere summer upper-tropospheric circulation? *Climate Dyn.,* **37,** 1189–1203, doi:10.1007/s00382-010-0909-9.

——, ——, M. C. Wheeler, X. Fu, D. E. Waliser, and I.-S. Kang, 2013: Real-time multivariate indices for the boreal summer intraseasonal oscillation over the Asian summer monsoon region. *Climate Dyn.,* **40,** 493–509, doi:10.1007/s00382-012-1544-4.

Meehl, G. A., and H. Teng, 2007: Multi-model changes in El Niño teleconnections over North America in a future warmer climate. *Climate Dyn.,* **29,** 779–790, doi:10.1007/s00382-007-0268-3.

——, and Coauthors, 2007: Global climate projection. *Climate Change 2007: The Physical Science Basis,* S. Solomon et al., Eds., Cambridge University Press, 747–846.

Moon, J.-Y., B. Wang, K.-J. Ha, and J.-Y. Lee, 2013: Teleconnections associated with Northern Hemisphere summer monsoon intraseasonal oscillation. *Climate Dyn.,* **40,** 2761–2774, doi:10.1007/s00382-012-1394-0.

North, G. R., T. L. Bell, R. F. Cahalan, and F. J. Moeng, 1982: Sampling errors in the estimation of empirical orthogonal function. *Mon. Wea. Rev.,* **110,** 699–706, doi:10.1175/1520-0493(1982)110<0699:SEITEO>2.0.CO;2.

Seo, K.-H., J. Ok, J.-H. Son, and D.-H. Cha, 2013: Assessing future changes in the East Asian summer monsoon using CMIP5 coupled models. *J. Climate,* **26,** 7662–7675, doi:10.1175/JCLI-D-12-00694.1.

Smith, T. M., and R. W. Reynolds, 2004: Improved extended reconstruction of SST (1854–1997). *J. Climate,* **17,** 2466–2477, doi:10.1175/1520-0442(2004)017<2466:IEROS>2.0.CO;2.

Stevenson, S., B. Fox-Kemper, M. Jochum, R. Neale, C. Deser, and G. Meehl, 2012: Will there be a significant change to El Niño in the twenty-first century? *J. Climate,* **25,** 2129–2145, doi:10.1175/JCLI-D-11-00252.1.

Taylor, K. E., R. J. Stouffer, and G. A. Meehl, 2012: An overview of CMIP5 and the experiment design. *Bull. Amer. Meteor. Soc.,* **93,** 485–498, doi:10.1175/BAMS-D-11-00094.1.

Wallace, J. M., E. M. Rasmusson, T. P. Mitchell, V. E. Kousky, E. S. Sarachik, and H. von Storch, 1998: On the structure and evolution of ENSO-related climate variability in the tropical Pacific: Lessons from TOGA. *J. Geophys. Res.,* **103,** 14 241–14 259, doi:10.1029/97JC02905.

Wang, B., 1995: Interdecadal changes in El Nino onset in the last four decades. *J. Climate,* **8,** 267–258, doi:10.1175/1520-0442(1995)008<0267:ICIENO>2.0.CO;2.

——, J. Yang, T. Zhou, and B. Wang, 2008: Interdecadal changes in the major modes of Asian–Australian monsoon variability: Strengthening relationship with ENSO since the late 1970s. *J. Climate,* **21,** 1771–1789, doi:10.1175/2007JCLI1981.1.

——, and Coauthors, 2009: Advance and prospectus of seasonal prediction: Assessment of the APCC/CliPAS 14-model ensemble retrospective seasonal prediction (1980–2004). *Climate Dyn.,* **33,** 93–117, doi:10.1007/s00382-008-0460-0.

——, B. Xiang, and J.-Y. Lee, 2013: Subtropical high predictability establishes a promising way for monsoon and tropical storm prediction. *Proc. Natl. Acad. Sci. USA,* **110,** 2718–2722, doi:10.1073/pnas.1214626110.

——, S.-Y. Yim, J.-Y. Lee, J. Liu, and K.-J. Ha, 2014: Future change of Asian-Australian monsoon under RCP 4.5 anthropogenic warming scenario. *Climate Dyn.,* **42,** 83–100, doi:10.1007/s00382-013-1769-x.

Wang, H., B. Wang, F. Huang, Q. Ding, and J.-Y. Lee, 2012: Interdecadal changes of the boreal summer circumglobal teleconnection (1958–2010). *Geophys. Res. Lett.,* **39,** L12704, doi:10.1029/2012GL052371.

Weare, B. C., 2013: El Niño teleconnections in CMIP5 models. *Climate Dyn.,* **41,** 2165–2177.

Xiang, B., B. Wang, A. Lauer, J.-Y. Lee, and Q. Ding, 2014: Upper tropospheric warming intensifies sea surface warming. *Climate Dyn.,* doi:10.1007/s00382-013-1928-0, in press.

Xie, P., and P. A. Arkin, 1997: Global precipitation: A 17-year monthly analysis based on gauge observations, satellite estimates, and numerical model outputs. *Bull. Amer. Meteor. Soc.,* **78,** 2539–2558, doi:10.1175/1520-0477(1997)078<2539:GPAYMA>2.0.CO;2.

Yeh, S.-Y., J.-S. Kug, B. Dewitte, M.-H. Kwon, B. P. Kirtman, and F.-F. Jin, 2009: El Niño in a changing climate. *Nature,* **461,** 511–514, doi:10.1038/nature08316.